Exploring the Potential of Perovskite/Perovskite/Silicon Triple-Junction Pv Modules in Two- and Four-Terminal Configuration

Blom, Youri; Vogt, Malte Ruben; Uzu, Hisashi; Koizumi, Gensuke; Yamamoto, Kenji; Isabella, Olindo; Santbergen, Rudi

DOI
10.1002/solr.202400613

Publication date
2025

Document Version
Final published version

Published in
Solar RRL

Solar RRL

WILEY VCH

Solar RRL

RESEARCH ARTICLE OPEN ACCESS

Exploring the Potential of Perovskite/Perovskite/Silicon Triple-Junction Pv Modules in Two- and Four-Terminal Configuration

Youri Blom[1] | Malte Ruben Vogt[1] | Hisashi Uzu[2] | Gensuke Koizumi[2] | Kenji Yamamoto[2] | Olindo Isabella[1] | Rudi Santbergen[1]

[1]Photovoltaic Materials and Devices Group, Delft University of Technology, Delft, The Netherlands | [2]Kaneka Corporation, Osaka, Japan

Correspondence: Youri Blom (y.blom@tudelft.nl) | Rudi Santbergen (r.santbergen@tudelft.nl)

Received: 22 August 2024 | **Revised:** 17 January 2025 | **Accepted:** 27 January 2025

Funding: New Energy and Industrial Technology Development Organization, Grant/Award Number: JPNP20015

Keywords: bandgap engineering | energy yield simulations | optoelectrical simulations | perovskite/silicon | triple-junction solar cells

ABSTRACT

In the quest for advancing photovoltaic efficiency, the adoption of multijunction solar cell architectures has emerged as a promising approach. Perovskite/silicon double-junction solar cells have already achieved efficiencies surpassing 33%, exceeding the theoretical efficiency limit for single-junction devices. To enhance efficiency even further, exploring perovskite/perovskite/silicon (PPS) triple-junction solar cells seems a logical next step, as they offer the potential to further reduce thermalization losses and achieve even higher efficiencies. This study delves into the potential of various configurations of PPS modules, exploring different subcell interconnections. Initially, we present an optoelectrical model to simulate the performance of these devices, incorporating both luminescence coupling and cell-to-module losses. This enables us to optimize the bandgap energy of the top and middle perovskite subcells under both standard test conditions (STC) and outdoor conditions. Our analysis reveals that the addition of a perovskite subcell can improve the STC efficiency up to 9%–13%. This gain in STC performance also translates into a similar gain in energy yield, meaning that triple-junction devices produce 8%–14% more electricity than their double-junction reference devices.

1 | Introduction

Conventional crystalline silicon (c-Si) cells have reached record cell efficiencies of 27.3% [1], approaching the efficiency limit of 29.4% for c-Si [2, 3]. To further increase solar cell efficiencies, perovskite/silicon (PS) tandem solar cell technologies stand out as promising contenders for the next generation of photovoltaic (PV) modules. Tandem cells incorporating perovskite and silicon have already achieved a record efficiency of 34.6% [4], surpassing the theoretical efficiency of c-Si. Moreover, studies by Zafoschnig et al. suggest that perovskite silicon tandem modules could significantly decrease the levelized cost of electricity in PV technology by 10%–20% [5], pointing toward a substantial market share for silicon-based tandems by 2033 [6]. Numerous studies have investigated the performance and energy yield of double-junction modules [7–13], showing that tandem modules can have significantly higher energy yield than single-junction devices.

Although double-junction cells have achieved an impressive record efficiency, they still have a practical and theoretical cell efficiency limit of 39.5% [14] and 42% [15, 16], respectively. Even higher efficiencies can be obtained by adding an additional perovskite subcell, creating a triple-junction perovskite/perovskite/silicon (PPS) cell. This triple-junction technology has already been fabricated on cell level in literature [17–23] with a record cell efficiency of 27.1% [24]. Restat et al. have demonstrated that this technology holds a practical cell efficiency limit

of 44.3% [25], suggesting that triple-junction tandem devices can potentially outperform double-junction devices.

It should be realized that module efficiencies are typically smaller than cell efficiencies due to nonactive areas, glass coverage, and interconnection losses [26]. Additionally, the outdoor operating conditions are very different compared to the standard test conditions (STC), which can significantly change the performance, especially for tandem devices [27]. To the best of the authors' knowledge, the potential performance of PPS tandem modules at STC and outdoor operating conditions has not been explored yet.

This study delves into the potential of triple-junction technology by simulating the performance of PPS modules. Building upon our previous work [28], designed for energy yield simulations of double-junction modules, we perform optoelectrical simulations for simulating triple-junction modules. Optimization of bandgap energies for both perovskite subcells is crucial, given the importance of current matching. Additionally, we analyze various four-terminal (4T) module configurations, alongside the more typical two-terminal (2T) configuration. In conclusion, energy yield simulations for both double- and triple-junction modules are performed to uncover the potential of triple-junction PV modules.

2 | Methodology

For double-junction devices, subcells can be arranged either in a series connection or operate independently, representing the 2T and 4T configurations. In the case of triple-junction devices with three subcells, the number of possible connections is more extensive. In this study, we explore three distinct configurations, as illustrated in Figure 1:

- The perovskite–perovskite/silicon (P-PS) device is a 4T module, where the middle perovskite and silicon sub-cells are connected in series, allowing the top perovskite cell to operate independently.
- The perovskite/perovskite–silicon (PP-S) device is also a 4T module, but with a series-connected top and middle perovskite cell, meaning that the silicon cell operates independently.
- The perovskite/perovskite/silicon (PPS) device is a 2T module where all subcells are connected in series.

In the notation, we use a "-" to denote electrically unconnected cells, while for series-connected tandem subcells, the letters follow directly. To assess the impact of the third subcell, we also evaluate the performance of a perovskite–silicon (P-S) 4T and perovskite/silicon (PS) 2T double-junction devices as reference. The P-PS and PP-S architectures can be seen as extensions of the P-S 4T device, where an additional perovskite cell is added to the bottom (P-PS) or top (PP-S) cell. Similarly, PPS 2T can be seen as an extension of the PS 2T reference.

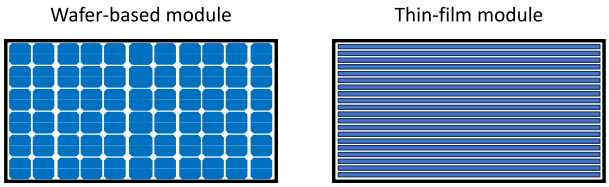

FIGURE 2 | The geometry of the wafer-based and thin-film modules.

The PV modules of four-terminal devices will consist of two submodules separated by the encapsulant. An important distinction must be made between these two submodules, as they are based on a different cell technology. For all 4T devices, the top submodule consist of perovskite cells only, meaning the submodule will be similar to a thin-film module. The perovskite cells in these submodules consist of long narrow strips, that are separated by laser scribes [29–33]. On the contrary, the bottom submodule consists of a silicon wafer on which the other layers are deposited, meaning that the submodule is wafer-based. The difference between the two modules is illustrated in Figure 2. It should be noted that 4T devices potentially need two separate inverters. However, our work only considers DC-generated electricity, so this is not included in the comparison. The 2T devices will all be wafer-based modules, as the perovskite subcells are deposited on the silicon wafer.

We also explore the impact of configuring the modules as bifacial, enabling irradiance from both the front and rear sides. Studies on c-Si modules have indicated that this rear irradiance could potentially enhance energy yield by up to 40% [34, 35]. In existing literature, it has been demonstrated that configuring perovskite/silicon modules as bifacial influences the optimal bandgap energy for the perovskite layer [9–11, 36–39]. Therefore, we perform bandgap energy optimizations for monofacial and bifacial PPS modules to analyze their differences.

The simulation of the different modules is separated into an optical and electrical part. An overview of the methodology is shown in Figure 3. We start by detailing the optical simulations, followed by an explanation of our electrical simulations. To validate our approach, we simulate a PS 2T tandem cell from literature and compare the results to the experimental data.

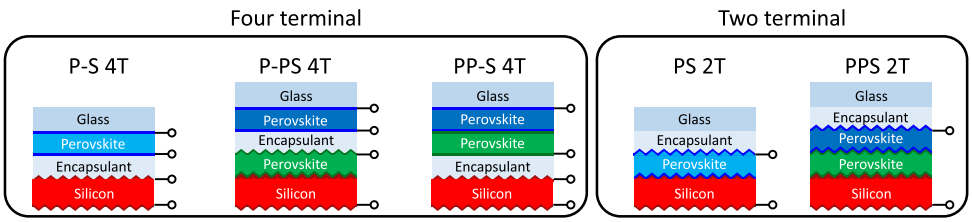

FIGURE 1 | An overview of the tested configurations. We have two double-junction reference devices and three triple-junction devices. The triple-junction devices are labeled with P-PS, PP-S, and PPS.

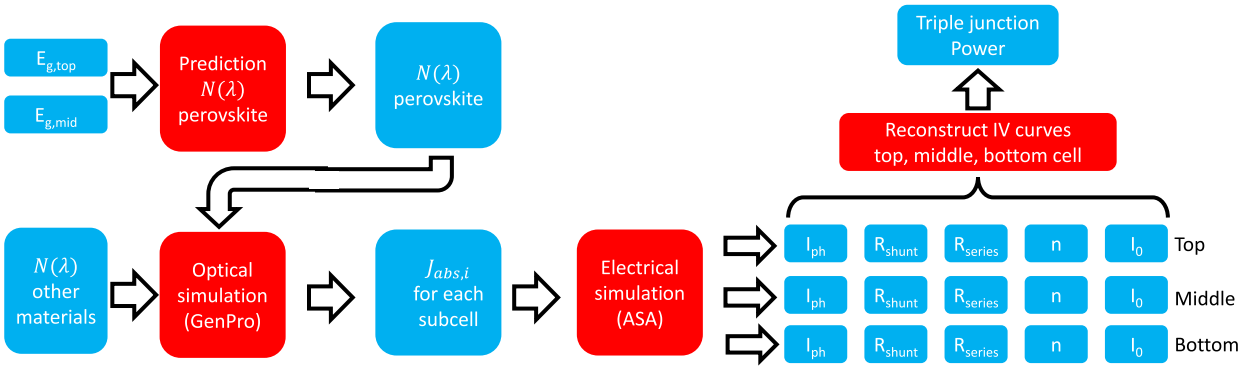

FIGURE 3 | An overview of the methodology used in this work. The red boxes indicate the different models that are used, and the blue boxes represent the inputs and outputs of all models. First, a bandgap energy for the top and middle cell need to be selected, which is used to predict their complex refractive index ($N(\lambda)$). Then, optical and electrical simulations are performed to calculate the power of the triple-junction device.

2.1 | Optical Simulations

We conduct the optical simulations using GenPro [40], which employs the net radiation method [41]. GenPro takes the complex refractive index ($N(\lambda) = n(\lambda) + j.k(\lambda)$) and the thickness ($d$) of each layer as input, producing the spectral absorptance ($A_i(\lambda)$) of the absorber layer for each subcell i. The calculated $A_i(\lambda)$ represents the fraction of absorbed photons at wavelength λ and allows us to compute the absorbed current density ($J_{abs,i}$) in each subcell using

$$J_{abs,i} = q \cdot \int A_i(\lambda) \cdot \phi_{in}(\lambda) d\lambda \quad (1)$$

where q represents the charge of an electron, and $\phi_{in}(\lambda)$ is the incident photon flux. The computed $J_{abs,i}$ values are input for the subsequent electrical simulations, as depicted in Figure 3.

2.1.1 | Refractive Index for Perovskite

As mentioned earlier, GenPro requires $N(\lambda)$ for all materials. The refractive index of perovskite is affected by the selected bandgap energy for the top and middle perovskite cell, as shown in Figure 3. To optimize the bandgap energy (E_g) of both perovskite layers, we need the refractive index of perovskite for each value of E_g. We use the measured data from Manzoor [42] to predict $N(\lambda)$ for perovskite for arbitrary bandgap energies, utilizing the approach outlined in our prior work [43, 44]. This method allows us to use one consistent $N(\lambda)$ data set in the entire bandgap range 1.2–2.4 eV. Note that the data near the edge of this range might be less accurate as it is based on extrapolation. However, in the most relevant range (1.4–1.9 eV) where we find the optimum bandgaps, the data can be considered most accurate. The $n(\lambda)$ and $k(\lambda)$ for different values of E_g are shown in Figure 4. Note that steps of 0.1 eV are shown, but our interpolation method allows arbitrarily small steps. The complex refractive index of perovskite for all bandgap energies can be found in the Supporting Information.

2.1.2 | Luminescence Coupling

Not all generated electron–hole pairs will be collected at the contacts. Some will radiatively recombine and generate photons with an energy equal to E_g. In multijunction solar cells, the photons emitted by a high-bandgap subcell can be re-absorbed by lower-bandgap subcells, which is known as photon recycling [45–48]. In this study, we use GenPro simulations, similar to the method developed by Jäger et al. [36] to incorporate this effect. The luminescence efficiency $\eta_{LC,i\to h}$, representing the fraction of recombined current in subcell i that translates into a photon absorption in subcell h, is calculated using

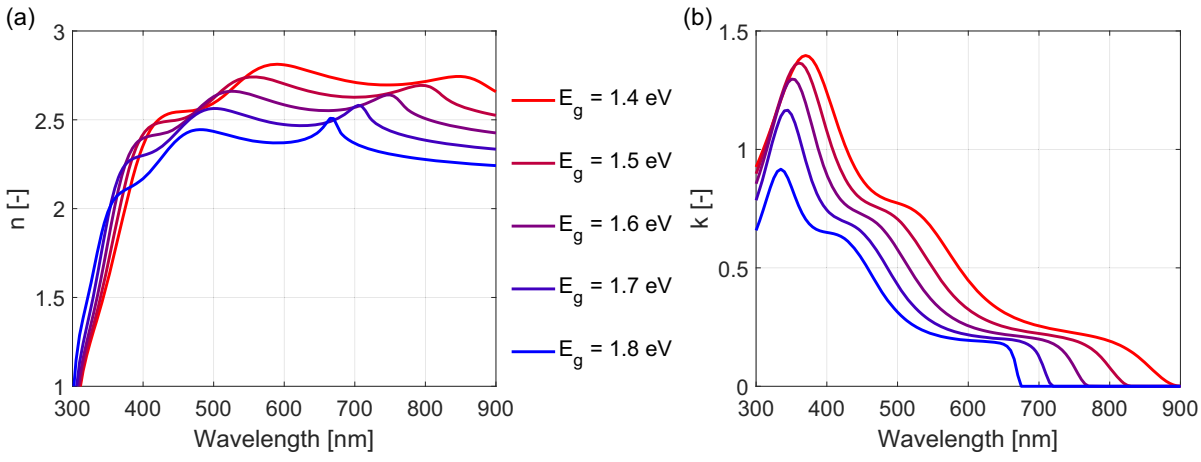

FIGURE 4 | The simulated complex refractive index of perovskite with different bandgap energies. (a) and (b) show $n(\lambda)$ and $k(\lambda)$ for each value.

$$\eta_{\mathrm{LC},i\to h} = \frac{\mathrm{ILQE}\cdot A_{i\to h}}{1-\mathrm{ILQE}\cdot A_{i\to i}} \tag{2}$$

where ILQE denotes the internal luminescence quantum efficiency, indicating the fraction of recombined electron–hole pairs that recombine radiatively. In our work, ILQE is set to 65%, a value derived by Jäger et al. [36]. The terms $A_{i\to h}$ represent the fraction of photons emitted from subcell i that is absorbed in subcell h, which is calculated using GenPro [40]. Similarly, $A_{i\to i}$ represents the fraction of photons emitted from subcell i that is absorbed in subcell i itself, respectively. Further details on the method for incorporating photon recycling and the derived values for $\eta_{\mathrm{LC},i\to h}$ can be found in the Supporting Information.

2.1.3 | Optical Layer Structures

The structures of simulated double- and triple-junction modules are illustrated in Figure 5. We assume that the silicon wafers (shown in gray) are textured on both sides. The texture morphology is conformally transferred to the next interface after the deposition of subsequent layers.

In the four-terminal configurations, consisting of two submodules, the encapsulation is positioned between the submodules, indicating that perovskite deposition occurs on glass for thin-film modules. In contrast, all perovskite subcells are deposited on the silicon cell for the two-terminal configurations. These specific structures serve as input for GenPro to compute the spectral absorptance of each layer. The references to the complex refractive index of all materials can be found in the Supporting Information. It should be noted that Figure 5 shows the structure of the monofacial devices. The structures of the bifacial ones are shown in the Supporting Information.

For the four terminal devices, both the n-*i*-p and p-*i*-n configurations are possible for the top submodule. In the supporting information, we have compared the optical response of both configurations. Since the n-*i*-p configuration has a better optical performance, this configuration is used in this work.

2.2 | Electrical Simulations

As shown in Figure 3, the results of the optical simulations are used as input for the electrical simulations. First, the electrical performance is simulated at cell level by calculating the current–voltage (*IV*) curves of every cell. Then, the module performance is estimated by interconnecting the cells and including cell-to-module losses, such as nonactive area and interconnection resistances.

2.2.1 | Cell Performance

The electrical performance is simulated following the approach outlined by Vogt et al. [28]. Initially, the Advanced Semiconductor Analysis (ASA) software [49] calculates the IV curves for each individual subcell under varying irradiance and temperatures. ASA simulates these *IV* curve by solving the Poisson and continuity equations in one dimension. Subsequently, a one-diode equivalent circuit model is employed to fit all *IV* curves, resulting in a Calibrated Lumped Element Model (CLEM) where all parameters are a function of both temperature and illumination conditions. These five parameters are the photogenerated current (I_{ph}), the saturation current (I_0) and the ideality factor (n) of the diode, the shunt resistance (R_{sh}), and the series resistance (R_{s}). The current density–voltage (*JV*) curves of the perovskite subcells with different bandgap energies are shown in Figure 6a. The full details of the input parameters used for the electrical simulations are provided in the Supporting Information.

As discussed earlier, emitted photons in high-bandgap subcells can be re-absorbed in lower-bandgap subcells. This is illustrated in Figure 6b, where a fraction of the recombination current, $\eta_{LC,i\to h}\,(I_{\mathrm{ph},i}-I_i\,(V_i))$, contributes to a larger current in other cells. To include this effect in the electrical simulations, I_{ph} is corrected for subcells below a high-bandgap cell, using a similar approach as Jäger et al. [36]

$$I_{\mathrm{ph},2} = I_{\mathrm{ph}0,2} + \eta_{LC,1\to 2}\left(I_{\mathrm{ph},1} - I_1(V_1)\right) \tag{3}$$

and

$$I_{\mathrm{ph},3} = I_{\mathrm{ph}0,3} + \eta_{\mathrm{LC},1\to 3}\left(I_{\mathrm{ph},1} - I_1(V_1)\right) + \eta_{\mathrm{LC},2\to 3}\left(I_{\mathrm{ph},2} - I_2(V_2)\right) \tag{4}$$

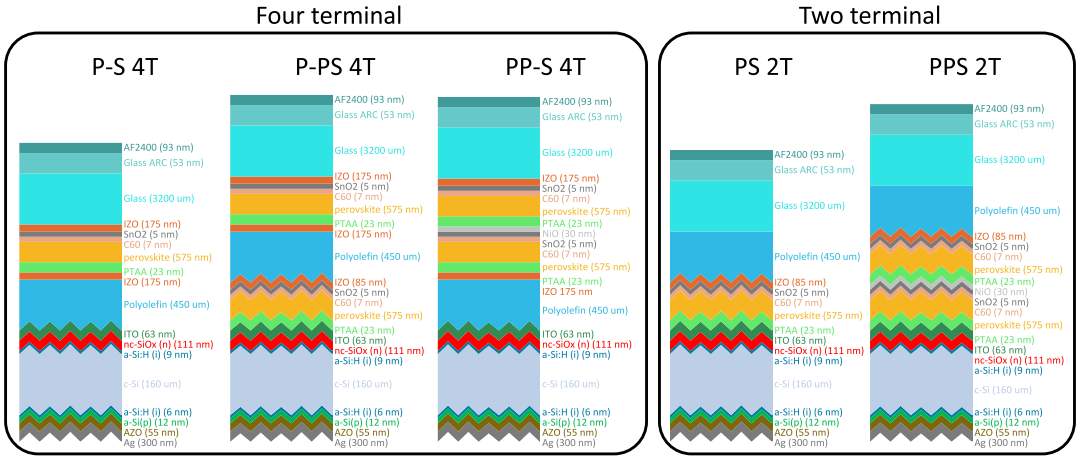

FIGURE 5 | The optical structures for all monofacial modules that are used as input in GenPro.

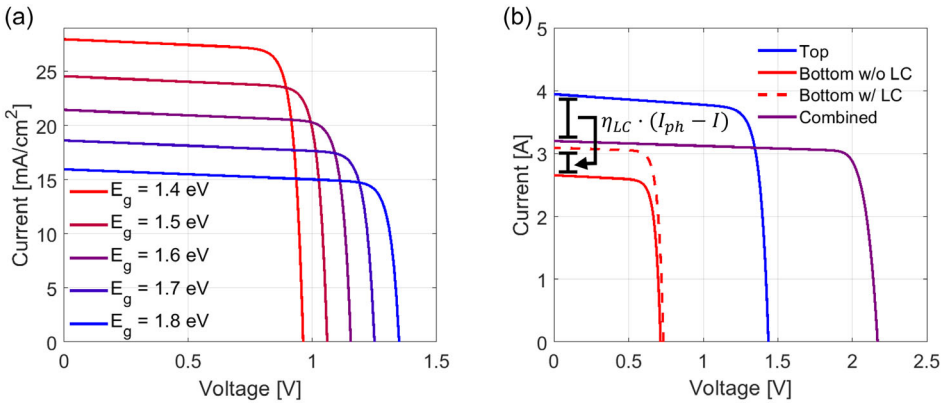

FIGURE 6 | (a) The *JV* curves of the perovskite subcells for the different bandgap energies. It should be noted that these curves correspond to an independent perovskite cell under STC conditions. (b) An illustration of photon recycling in the PS 2T device. A part of the recombined current can contribute to the current in the bottom cell.

where $I_{\mathrm{ph},i}$ is the I_{ph} of subcell i, $I_{\mathrm{ph0},i}$ is the original I_{ph} of subcell i when excluding luminescence coupling, and $I_i\ (V_i)$ is the output current of subcell i at its operating voltage. In Equation 3 and 4, all $\eta_{i\to h}$ are independent of the operating conditions of the module, but only the recombined current depends on the operating conditions.

As shown in Figure 1, several modules operate in a 4T configuration, meaning that submodules operate at different currents. As photon recycling depends on the operating current, it would mean that the maximum power point current of one submodule can be influenced by the other submodules, making the implementation more complicated. To simplify the methodology, we only consider luminescence coupling between subcells within the same submodule. This assumption is justified by the fact that $\eta_{\mathrm{LC},i\to h}$ consistently remains below 0.1 when i and h belong to different submodules, as demonstrated in the Supporting Information. Thus, we can disregard the impact of luminescence coupling on the absorbed photons in such scenarios.

2.2.2 | Subcell Interconnection

Figure 7 illustrates the electrical connections of the simulated monofacial devices. As detailed in the preceding section, each subcell is simulated using a one-diode equivalent circuit model. The subcells are interconnected according to the configuration depicted in Figure 1, with interconnection resistances introduced in each submodule.

As shown in Figure 7, resistances are added at the connections to represent the losses caused by the lateral current collection. This will be further explained in the next section. In the case of bifacial modules, these additional resistances are also incorporated on the rear side to account for the rear metalization needed for bifacial cells. The electrical interconnections of the bifacial modules are shown in Supporting Information.

2.2.3 | Module Performance

PV modules typically experience the so-called cell-to-module (CTM) losses, which are caused by the interconnection of the different cells into a module. In this work, we include the following CTM losses

- Additional optical losses due to the glass coverage and encapsulant
- Active area losses
- Ohmic interconnection losses

The additional optical losses are already included in the optical model, as the structures in Figure 5 include the glass coverage. As mentioned before, modules consisting of four terminals

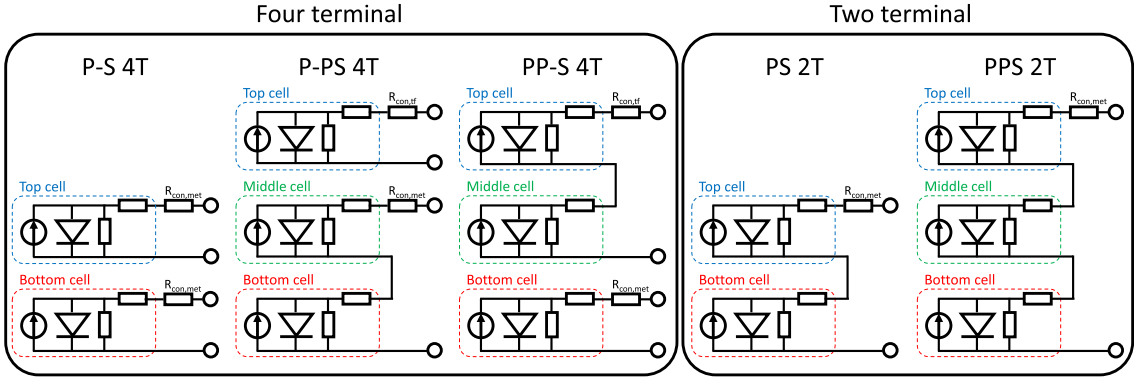

FIGURE 7 | The interconnection of the different simulated modules.

contain a thin-film and a wafer-based submodules. Although the implementation of the CTM losses in both submodule types is very similar, it is important to note that they have different causes.

In wafer-based modules, ohmic losses arise due to the metallization required for current collection. Jung et al. [50] have calculated this resistance to be 3.9 mΩ for c-Si cells. To address these ohmic losses, a resistor ($R_{\text{con, met}}$) is introduced into the equivalent circuit, as shown in Figure 7. Additionally, metallization induces shading on the cells, reducing the cell's active area. This shading effect is incorporated by introducing a shading factor ($S_{\text{f, waf}}$). The cell's current (I_{out}) is then adjusted using

$$I_{\text{out}} = \left(1 - S_{\text{f,waf}}\right) \cdot A_{\text{cell}} \cdot J_{\text{act}} \tag{5}$$

where A_{cell} is the area of the cell and J_{act} is the current density of the active area of the cell. Our work assumes $S_{\text{f, waf}}$ to be 2% for wafer-based modules. This is based on a typical metal coverage of 5% [51] and an optical factor of approximately 40% [52]. In thin-film modules, cells are connected through laser scribing, which reduces the active area's effectiveness in capturing photons. To counteract this optical loss, we incorporate a shading factor ($S_{\text{f,TF}}$) for thin-film modules, calculated as:

$$S_{\text{f,TF}} = 1 - \frac{L_{\text{act}}}{L_{\text{act}} + 2 \cdot L_{\text{sf}} + P_1 + P_2 + P_3} \tag{6}$$

where L_{act} is the active area width, L_{sf} is the safety area, and P_1, P_2, P_3 are the width of the different laser scribes [29]. Utilizing optimized values determined by Castriotta [29], we derive $S_{\text{f,TF}} = 8\%$. Moreover, thin-film modules encounter ohmic losses as the charge carriers need to be transported from one cell to the other via the ITO layer. In our study, we assume a resistance of 77 mΩ, as detailed in the Supporting Information. In practice, the dead area of a thin film module can be more transparent than the active area, as it consists of a transparent conductive oxide (TCO). This can allow more light to be transmitted to the underlying submodule, working as a gain factor for other subcells. However, this is excluded from our model, as this is a relatively small effect, and it would make the simulation significantly more complex. In the Supporting Information, we have estimated the effect of including this effect.

The shading factors and interconnection resistances used are primarily based on single-junction devices. Since tandem devices share current across subcells, the overall current will be lower, which may require different considerations. To evaluate the importance of these parameters, a sensitivity analysis is provided in the Supporting Information.

2.2.4 | Geometry of the Modules

Since the tested module types have either two or four terminals, their designs also differ. P-PS 4T and PP-S 4T comprise both a wafer-based and a thin-film submodule, while PPS 2T consists of just a wafer-based module. Since the submodules eventually need to be mounted together in one frame, both submodules maintain the need to have identical sizes. The dimensions of each module are outlined in Table 1. The width of the thin-film cells is set at 5.029 mm, a value determined to be optimal by Castriotta [29], which was also used in the calculation of cell-to-module losses. An illustration of both module types is shown in Figure 2.

2.3 | Energy Yield Simulation

To simulate the energy yield of the different modules, the above-described methodology is included in the PVMD Toolbox [28], which is a modeling framework for PV modules under outdoor conditions. As fully explained by Vogt et al. [28], the Toolbox separates the energy yield calculation into different steps. First, it simulates the optical response of the module to determine the received irradiance and cell temperature for every hour of the year. Then, it calculates the electrical performance to obtain the annual energy yield. In our simulations, we assume that the bandgap energy (E_g) is independent of temperature. However, in reality, the bandgap energy of perovskite increases with temperature due to changes in the lattice constant, as shown by Moot et al. [53]. This increase in E_g would lead to a slight reduction in current absorption, though the change in J_{sc} is less than 0.05%/°C, as measured by Moot et al. [53].

Since Vogt et al.'s work [28], the PVMD Toolbox has undergone several extensions and improvements. A new backward ray-tracing model [54] has been implemented to reduce the computational time of incoming irradiance calculation. Additionally, the spectral irradiance model has been updated to SBDART [55], which distinguishes between direct and diffuse irradiance as well as between clear sky and cloudy conditions. A detailed explanation and the validation on the modeling of the spectral irradiance can be found in the Supporting Information. For this work, we conduct a free horizon environment when simulating outdoor performance.

2.4 | Validation

We validate our method by simulating the 32.5% efficient PS tandem cell of HZB [56] and the 27.1% efficient PPS tandem cell of Liu [24]. Figure 8a shows the measured and simulated absorption of the top and bottom cell in the PS device, showing that our

TABLE 1 | The geometry of the wafer-based and thin-film modules.

Submodule type	Number of cells	Cell size [mm] (length × width)	Cell spacing [mm]	Edge spacing [mm]	Module size [mm] (length × width)
Wafer-based	72	156.75 × 156.75	3	10	1930 × 975.5
thin-film	190	1914 × 5.029	0	10	1930 × 975.5

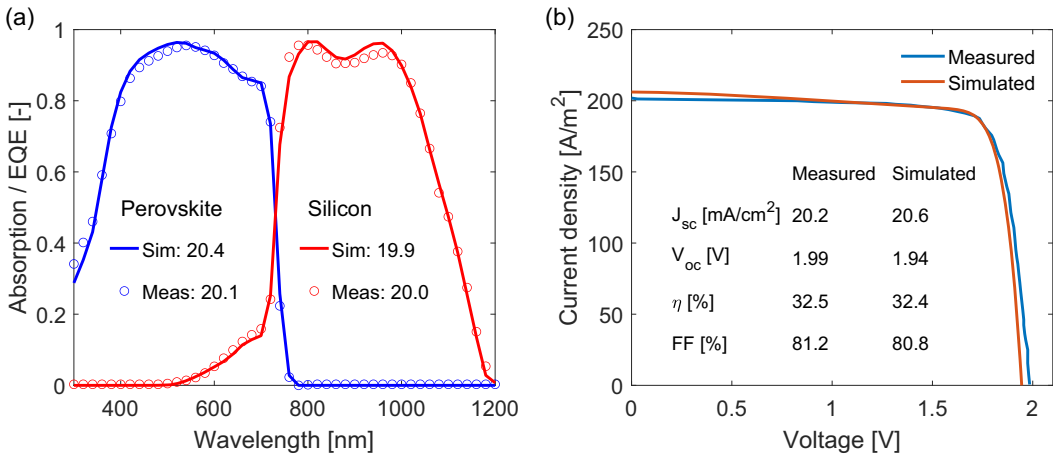

FIGURE 8 | (a) The optical validation by comparing the simulated absorptance with the measured EQE of the tandem cell from HZB [56]. The values inside the figure represent the absorbed current density in mA cm^{-2}. The diagram in (b) shows the electrical validation by comparing the simulated and measured JV curve.

optical model can accurately predict its absorption. The electrical validation of the PS cell is shown in Figure 8b, where our simulated *IV* curve closely matches the measured *IV* curve. Notably, there is a deviation in the open-circuit voltage (V_{oc}) and the short-circuit current density (J_{sc}). We believe that this is due to the fact that a one-diode model cannot fully capture the complete shape of the *IV* curve. Despite this, the deviation between the electrical characteristics of the measured and simulated IV curve is at most 3%.

Figure 9 shows the optical (a) and electrical (b) validation of the PPS tandem cell, showing good agreement between measurement and simulation. In the optical simulation, there is a minor discrepancy in the absorption profile of the top and bottom cells, which we attribute to the exact thicknesses of all layers not being reported. The thicknesses used in our simulations are reported in the Supporting Information. Nevertheless, the deviation in absorbed current densities remains within 5%. In the electrical simulation, there is a slight overestimation in V_{oc}. This can also be attributed to the fact that the one-diode model cannot capture the full shape of the IV curve. Still, all electrical characteristics are within 2% accuracy.

It is worth noting that the used parameters of the electrical simulation are slightly different for the triple-junction device. As the perovskite subcells in the PPS cell have a lower quality than the perovskite cell in the PS cell, a parallel diode is added to represent the additional losses at the interfaces. This is further explained in the Supporting Information. For the results in this work, the perovskite cell in the PS device is used as reference.

For outdoor simulations, the PVMD Toolbox has been validated for c-Si modules, as demonstrated by Vogt et al. [28], confirming the accuracy of both the thermal and irradiance models, which are similar for tandem and c-Si modules. However, due to the limited availability of comprehensive outdoor performance data for perovskite–silicon devices, the validation has so far been restricted to c-Si modules. We recommend that future research focus on further validating the outdoor modeling of perovskite–silicon devices as more qualitative and quantitative data becomes available.

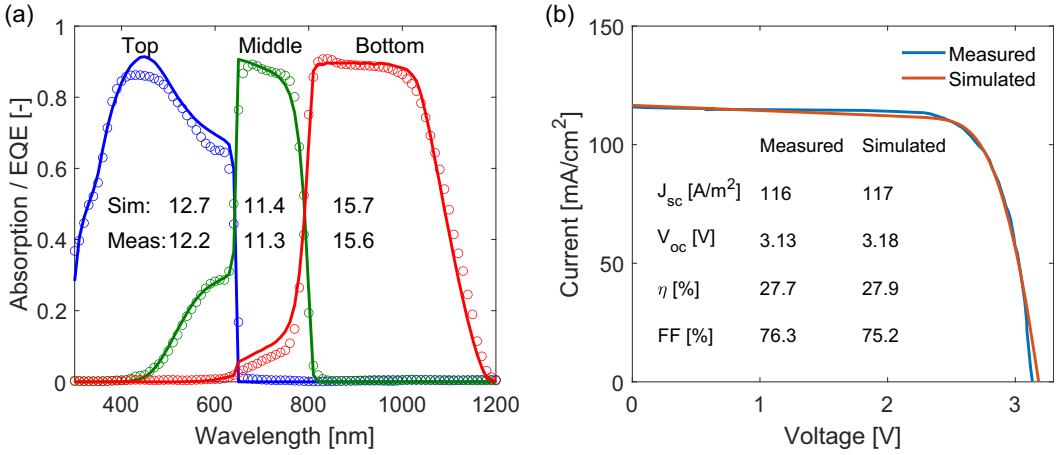

FIGURE 9 | (a) The optical validation by comparing the simulated absorptance with the measured EQE of the PPS cell from Liu [24]. The values inside the figure represent the absorbed current density in mA cm^{-2}. The diagram in (b) shows the electrical validation by comparing the simulated and measured *JV* curve.

3 | Operating Conditions

We quantify the performance of the different module types in both standard test and varying outdoor conditions. At STC, the modules operate in no wind at a temperature of 25°C and are exposed to the AM10.5 spectrum, containing an irradiance of 1000 W m^{-2}. For the bifacial modules, an additional rear-irradiance of 135 W m^{-2} is included according to the B-STC spectrum [57].

To study the outdoor performance, four geographical locations are selected, representing different climates according to the Köppen–Geiger-Photovoltaics (KGPV) classification [58, 59]. The selected locations are Delft (the Netherlands), Lagos (Nigeria), Lisbon (Portugal), and Shanghai (China). For each location, the climate data of a typical meteorological year (TMY) is obtained from Meteonorm [60]. Table 2 shows the most important characteristics of all locations.

An albedo of 20% is used for all locations, meaning that 20% of the irradiance reaching the ground will be diffusely reflected. Finally, the module geometry is kept the same for monofacial and bifacial modules.

4 | Results and Discussion

The outlined methodology is employed to find the maximum output power of various PPS modules at STC. We vary E_g for the top and middle perovskite cell from 1.20 to 2.40 eV in simulation steps of 0.05 eV. To obtain a higher resolution, we apply a cubic interpolation to reduce the stepsize to 0.01 eV. For both perovskite cells, a fixed thickness of 575 nm is used. Although the thickness is a parameter that can be adjusted for optimization, it would exponentially increase the number of simulations. Additionally, the perovskite thickness has a small impact on the maximum output power, as is demonstrated in the Supporting Information. Initially, we compared the STC performance of the various devices with different bandgap energies. Different losses are quantified to understand the differences between the different module types. Finally, we estimate the energy yield of the optimized modules for specified locations.

In our analysis, we use the module output power as metric rather than the module efficiency. The reason for this is that there are different irradiance levels for the mono- and bifacial modules, as discussed in Section 3. Using the module efficiency as metric can then lead to counterintuitive conclusions for the comparison between mono- and bifacial devices. Due to their higher irradiance level, bifacial modules can have lower efficiencies compared to monofacial ones, although their output power is higher.

4.1 | Simulating STC Performance

Figure 10 illustrates the output power for various modules with different bandgap combinations. The optimal bandgap energies are given in Table 3, showing that these are slightly lower for

TABLE 2 | The most important characteristics of the selected locations. The ambient temperature is weighted with the global horizontal irradiance. This metric is chosen as it, in our belief, better represents the operating conditions of the PV modules than the normal average of the ambient temperature. The selected module tilts are chosen such that they maximize the annual front-side irradiation for each location.

Location	Annual Global Horizontal Irradiation [kW h m^{-2}]	Weighted average ambient temperature [°C]	KPGV	Module tilt [°]
Delft	1018	16.2	DL	31
Lagos	1642	29.4	AH	5
Lisbon	1758	20.6	DH	28
Shanghai	1271	21.7	DM	17

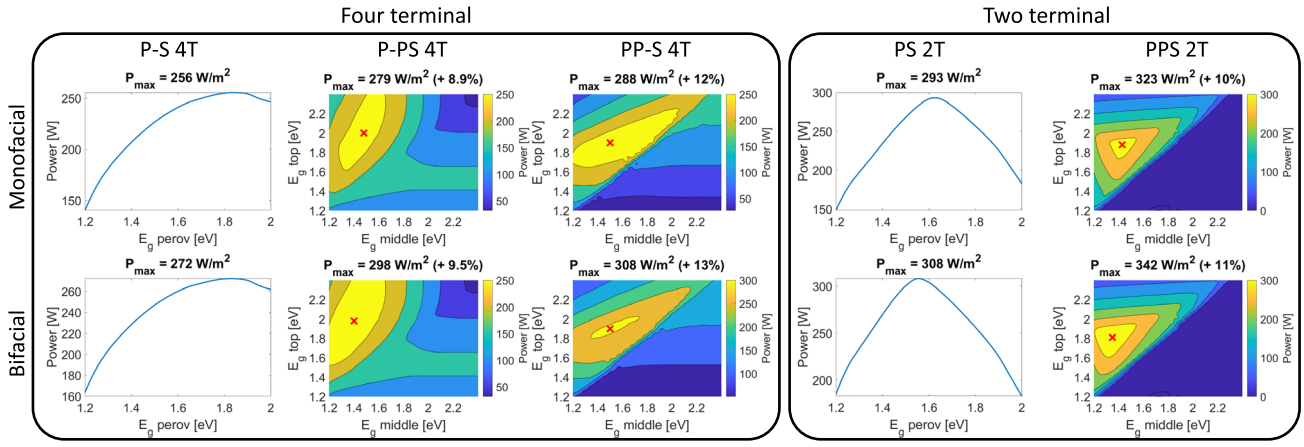

FIGURE 10 | The STC performance of the different PPS modules with different bandgap energies. For the PPS modules, the relative difference compared to their reference device is provided.

TABLE 3 | The optimal bandgap energies for the different modules.

Type	Monofacial $E_{g,top}$ [eV]	$E_{g,mid}$ [eV]	Bifacial $E_{g,top}$ [eV]	$E_{g,mid}$ [eV]
P-S 4T	1.84	–	1.83	–
P-PS 4T	2.00	1.48	1.98	1.40
PP-S 4T	1.90	1.50	1.90	1.50
PS 2T	1.62	–	1.56	–
PPS 2T	1.88	1.43	1.81	1.35

monofacial and bifacial modules. This is because the rear irradiance only affects the absorbed current in the bottom cell, changing the current matching conditions.

Given the large number of simulated architectures, numerous comparisons can be made. To maintain a structured discussion, we first compare the performance of the four-terminal and two-terminal reference double-junction modules. Next, we analyze the effect of adding a perovskite subcell by comparing the double- and triple-junction devices. Finally, we compare monofacial and bifacial modules to assess the impact of rear irradiance.

4.1.1 | Comparison 2T Versus 4T Double-Junction Modules

As shown in Table 3, for the double-junction modules, the P-S 4T module has a higher optimal E_g (1.84 eV) compared to the PS 2T one (1.62 eV). This difference is caused by the current requirements for the two-terminal device. As shown in the Supporting Information, the mismatch current is minimized at this bandgap energy, making it the optimal bandgap energy. Despite the current matching requirements, the two-terminal reference device (293 W m^{-2}) outperforms the four-terminal reference device (256 W m^{-2}). The difference in performance can largely be attributed to the CTM losses that are described in Section 2.2.3.

Figure 11 shows the spectral absorptance for top, middle, and bottom cell absorber layers. Also, the parasitic absorption and reflection losses are indicated. As can be seen in the figure, there are significantly lower reflection losses for the monolithic 2T devices. Due to the absence of texturing in the thin-film submodules, reflection is increased for the four-terminal devices, leading to reduced absorbed current in each subcell. Also, the additional TCO layers in the four-terminal modules increase the parasitic absorption. It should be noted, however, that the difference in current absorption in the perovskite for the PS 2T and P-S 4T is mostly due to the different bandgap energies, and not solely due to the increased reflection and parasitic absorption. A further quantification of the reflection and parasitic absorption losses can be found in the Supporting Information.

As shown in Figure 11, it appears that there are some current mismatches in series connect subcells. As example, the top and bottom cell in the PS 2T configuration have a 3.3 mA cm^{-2} difference in current absorption. However, the values in this figure report the optical absorption, excluding the effect of luminescence coupling. The electrical simulation does account for luminescence coupling, which effectively generates additional current in the current limiting subcell from the absorption of photons emitted from radiative recombination in the other subcells.

To quantify the effect of the other cell-to-module losses, we use the equations outlined in our prior research [16]. Figure 12 depicts the shading and interconnection losses for all configurations. As discussed in Section 2.2.3, the thin-film submodules in 4T modules have larger shading factors and interconnection resistances. This causes the CTM losses to be significantly greater than the monolithic 2T devices. Among the 4T devices, the P-PS module exhibits the lowest CTM losses. This is primarily because its design has the middle perovskite cell deposited onto the silicon wafer cell. Consequently, a larger portion of the power is generated by the wafer-based submodule. Since wafer-based submodules experience lower CTM losses compared to thin-film submodules, due to factors previously discussed, the P-PS configuration achieves reduced CTM losses compared to other 4T devices.

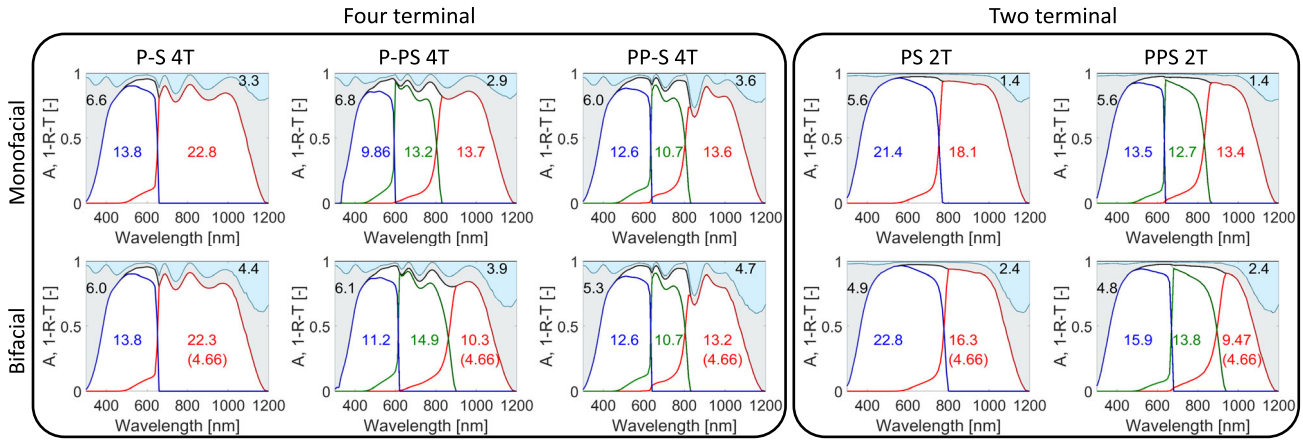

FIGURE 11 | The absorption profile of all the modules. Blue, green, and red represent the absorptance of the top, middle, and bottom absorber layers, respectively. The reflection and parasitic absorption are indicated with light blue and light gray respectively. Also, the current densities under the AM10.5 spectrum are shown in mA cm^{-2}, including the reflection (top right) and parasitic absorption (top left) current losses. Note that for the bifacial devices, the current density due of the rear irradiance is indicated with brackets.

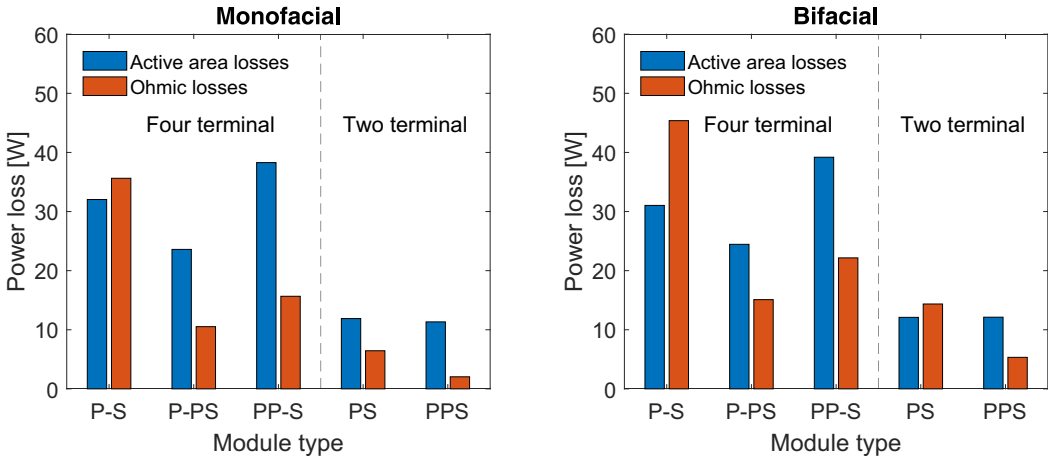

FIGURE 12 | The cell-to-module losses of the simulated modules.

4.1.2 | Comparison Double-Junction Versus Triple-Junction Modules

The performance of the double-junction devices can be improved by adding an additional perovskite subcell. As mentioned before, P-PS and PP-S 4T can be seen as extensions of the P-S 4T module, and PPS 2T as an extension of the PS 2T module.

Figure 10 shows that the P-PS 4T and PP-S 4T have an increase in power density of 9% and 13%, respectively. Although their optimal bandgap energies are very similar, the range of optimal bandgap energies is quite different. This is due to the different current requirements in both architectures, which is discussed in more detail in the Supporting Information. The increase of power for the PPS modules is not only due to the better spectral irradiance utilization (the fundamental advantage of triple junction over double junction), but also due to reduced CTM losses. Figure 12 shows that both ohmic interconnection losses are almost halved for the PPS devices. Because the irradiance spectrum is divided over three subcells instead of two, the output currents will be smaller. This reduces the ohmic losses and therefore improves the device performance.

The PPS 2T device has a gain in output power of 10%–11% compared to the PS 2T module, This gain is mostly attributed to better spectral utilization, but also lower ohmic interconnection losses (similar to the trend in four-terminal devices). PPS 2T reaches an output power density of 323 W m^{-2}, making this architecture the best performing one among those simulated. Due to the monolithic structure, it has lower optical losses than the other PPS modules (Figure 11).

Although PPS 2T has the highest performance of all triple-junction modules, it is noteworthy that PPS 2T only demonstrates optimal output power within a narrow range of bandgap energies, while P-PS 4T and PP-S 4T offer a broader range of bandgap energies with comparable performances. This indicates that the P-PS 4T and PP-S 4T provide more flexibility in the design of the perovskite subcells, which was also found by Futscher et al. [61].

4.1.3 | Comparison Monofacial Versus Bifacial

The last comparison for results under STC will be made between monofacial and bifacial devices. The B-STC spectrum has an additional 13.5% irradiance on the rear side. This 13.5% increase in irradiance translates into an increase in output power density by approximately 10% for all devices (Figure 10).

It is interesting to see that the optimal bandgap energies can vary quite significantly for bifacial modules compared to the monofacial ones. As the additional irradiance is only absorbed in the bottom cell, it can create a current mismatch in some architectures. Table 3 shows that $E_{g,mid}$ of P-PS 4T reduces from 1.48 to 1.40 eV when the module becomes bifacial. This decrease in bandgap energy allows the middle cell to absorb more irradiance, making the middle and bottom cell current matched. In the P-S 4T and PP-S 4T, the optimal bandgap energies are almost the same, since the bottom cell operates independently in both architectures. Therefore, the additional rear irradiance does not affect any current requirements.

For the two-terminal devices (PS 2T and PPS 2T), all subcells need to be current matched. Therefore, the optimal bandgap energies of all perovskite layers is significantly lower for these devices. It should be noted that in this case, luminescence coupling cannot compensate for the current mismatches. As the additional current is in the silicon bottom cell (with the lowest E_g), photon recycling is not possible. Also for the bifacial setting, the PPS 2T device has the highest performance among all simulated scenarios.

4.2 | Simulating Outdoor Performance

Lastly, we simulate the energy yield for different modules across various outdoor locations, using the STC-optimized bandgap configurations for these simulations. Since energy yield calculations are time-intensive, it is impractical to rerun simulations for each specific location. However, in reality, the optimal bandgap configuration might vary slightly from the STC configuration, as the spectrum of received irradiance can differ. Figure 13 shows the simulated energy yield of all modules at the different

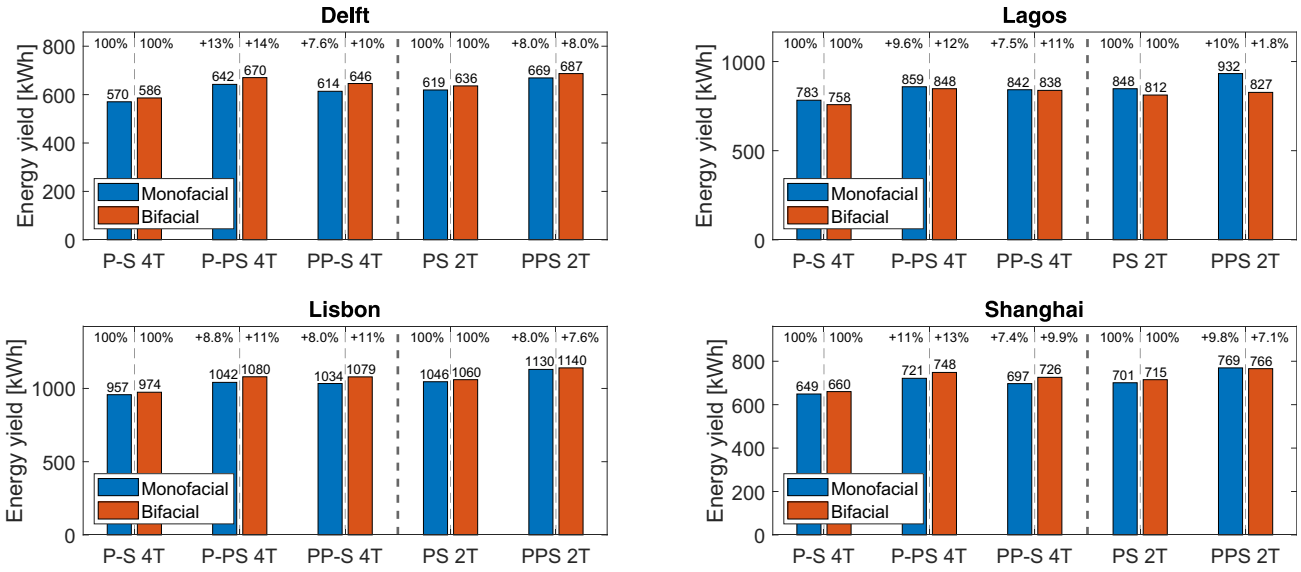

FIGURE 13 | The energy yield results for the different module types. The performance of the PS 2T and P-S 4T devices are used as reference, and the relative difference is shown for the PPS modules.

locations. Similar to the discussion of the STC results, we make the comparison between two- and four-terminal, double- and triple-junction, and monofacial and bifacial modules.

4.2.1 | Comparison 2T Versus 4T Double-Junction Modules

The energy yield production of the monofacial reference PS 2T and P-S 4T devices ranges from 619 to 1046 kWh and 570 to 957 kWh, respectively. For both modules, the highest energy yield is achieved in Lisbon as this location has the highest irradiance (Table 2).

The difference in performance between the 2T and 4T reference modules is caused by the same effects explained in the discussion on STC results. Due to increased reflection and higher interconnection resistances, the 4T modules experience greater CTM losses, limiting their performance.

4.2.2 | Comparison Double-Junction Versus Triple-Junction Modules

Figure 13 shows the relative gain of the triple-junction modules compared to their reference double-junction module. The monofacial P-PS 4T and PP-S 4T module experience a 8.8%–13% and 7.6%–8.0% gain in energy yield, respectively, compared to their reference P–S 4T module. Similarly, the monofacial PPS 2T module experiences a 8.0%–10% gain compared to its reference PS 2T module.

These results show that the gain achieved at the STC performance also translates into a similar gain under varying outdoor

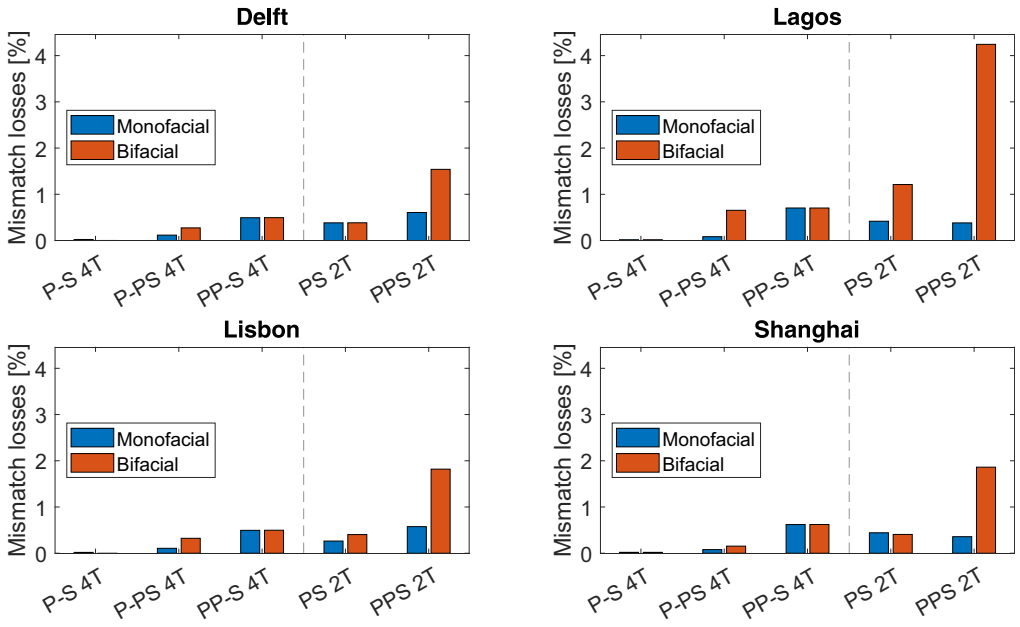

FIGURE 14 | The mismatch losses during the outdoor operation, quantified as a fraction of the total incoming irradiance.

conditions. This implies that the mismatch losses introduced by the third subcell are small than the gain in STC efficiency. Figure 14 shows the mismatch losses for all simulated scenarios. Mismatch losses are defined as the disparity between the sum of the individual maximum power from all subcells and the actual output power [16]. It can be seen that the mismatch losses are larger for the triple-junction modules compared to the double-junction one. For example, the mismatch losses of the PPS 2T device are approximately three times as large as those of the PS 2T device. Nevertheless, the figure shows that the mismatch losses of the monofacial PPS devices are maximally 0.5% compared to the total incoming irradiance.

4.2.3 | Comparison Monofacial Versus Bifacial

Finally, we can compare the energy yield performance of monofacial and bifacial devices. It is interesting to note that in some situations, monofacial devices produce a higher energy yield than bifacial devices. The bandgap energies of the bifacial modules are optimized under the B-STC irradiance spectrum, accounting for simultaneous front and rear irradiance of 1000 and 135 $W m^{-2}$, respectively. However, as the ray tracing simulations in the PVMD Toolbox show, these conditions rarely occur together, with front and rear irradiance peaking at different moments. This difference is detailed further in the Supporting Information. Since the rear irradiance is primarily absorbed in the bottom cell, the time profile of the rear irradiance only affects the bottom cell, resulting in differences between the absorbed current in the bottom subcell and the absorbed current in the top and middle subcells. Especially for the bifacial PPS 2T module, this significantly increases the mismatch losses (Figure 14), explaining why the monofacial PPS 2T module always outperforms its bifacial counterpart. It should also be noted that for Lagos, given its low module tilt of 5°, not much irradiance can reach the rear side. The lack of rear-side irradiance creates more mismatches, explaining why the monofacial modules outperform the bifacial ones. This suggests that the B-STC irradiance spectrum cannot be used for the optimization of double-junction or triple-junction devices.

5 | Conclusion

In conclusion, our study delves into the potential of triple-junction PPS modules. We have devised a methodology to simulate the optoelectrical performance of these devices, consisting of optical and electrical simulations. Our approach incorporates optical luminescence coupling between subcells and considers cell-to-module losses. Our methodology is integrated into the PVMD Toolbox, facilitating simulations of module performance under both STC and outdoor conditions. In the latter one, we conduct a horizon-free environment.

We compare three triple-junction module configurations, each with different subcell interconnections. Two configurations (P-PS and PP-S) employ four terminals, extending the two-junction 4T device, while one (PPS) is a two-terminal device, extending the two-junction 2T device. As a reference, our analysis also includes these two-junction PS 2T and P-S 4T modules.

Under STC conditions, we identify the optimal bandgap energies for the top and middle perovskite cells across different module types. For four-terminal modules, adding a third perovskite subcell can improve the STC performance by approximately 9% (P-PS) and 13% (PP-S). Two-terminal modules experience a 11% gain due to the additional perovskite subcell. Overall, the PPS 2T has the highest performance, as its monolithic configuration experiences lower optical and ohmic losses.

Under outdoor conditions, the gain in STC performance translates into a similar gain in the energy yield. The triple-junction modules produce 8%–14% more energy compared to their double-junction references.

Acknowledgments

This paper is partially based on results obtained from a project, JPNP20015, commissioned by the New Energy and Industrial Technology Development Organization (NEDO).

Data Availability Statement

The data that support the findings of this study are available from the corresponding author upon reasonable request.

References

1. *Longi Sets New World-Record for Silicon Solar Cell Efficiency, Launching 2nd Generation Ultra-Efficient bc-Based Module*, accessed August 21, 2024, https://www.longi.com/en/news/longi-hi-mo9-bc-world-record/.

2. A. Richter, M. Hermle, and S. W. Glunz, *IEEE Journal of Photovoltaics* 3, no. 4 (2013): 1184.

3. S. Schafer and R. Brendel, *IEEE Journal of Photovoltaics* 8, no. 4 (2018): 1156.

4. *6 Silicon-Perovskite Tandem Solar Cells*, accessed August 21, 2024, https://www.longi.com/en/news/2024-snec-silicon-perovskite-tandem-solar-cells-new-world-efficiency/.

5. L. A. Zafoschnig, S. Nold, and J. C. Goldschmidt, *IEEE Journal of Photovoltaics* 10, no. 6 (2020): 1632.

6. VDMA, International Technology Roadmap for Photovoltaics (itrpv) (2023).

7. M. T. Hörantner and H. J. Snaith, *Energy & Environmental Science* 10, no. 9 (2017): 1983.

8. Š. Tomšič, M. Jošt, K. Brecl, M. Topič, and B. Lipovšek, *Advanced Theory and Simulations* 6, no. 4 (2023): 2200931.

9. L. Xu, F. Xu, J. Liu, X. Zhang, A. S. Subbiah, and S. De Wolf, *ACS Energy Letters* 8, no. 7 (2023): 3114.

10. M. De Bastiani, A. J. Mirabelli, Y. Hou, et al., *Nature Energy* 6, no. 2 (2021): 167.

11. H. Hao, S.-T. Zhang, K. Wang, et al., *Solar RRL* 7 (2023): 15.

12. F. Gota, S. X. An, H. Hu, B. Abdollahi Nejand, and U. W. Paetzold, *Advanced Optical Materials* 11, no. 3 (2022): 2201691.

13. R. Schmager, M. Langenhorst, J. Lehr, U. Lemmer, B. S. Richards, and U. W. Paetzold, *Optics Express* 27, no. 8 (2019): A507.

14. O. Er-raji, C. Messmer, A. J. Bett, et al., *Solar RRL* 7 (2023): 24.

15. A. De Vos, *Journal of Physics D: Applied Physics* 13, no. 5 (1980): 839.

16. Y. Blom, M. R. Vogt, C. M. Ruiz Tobon, R. Santbergen, M. Zeman, and O. Isabella, *Solar RRL* 7, no 8 (2023): 2200579.

17. J. Werner, F. Sahli, F. Fu, et al., *ACS Energy Letters* 3, no. 9 (2018): 2052.

18. J. Zheng, G. Wang, W. Duan, et al., *ACS Energy Letters* 7, no. 9 (2022): 3003.

19. M. Heydarian, M. Heydarian, A. J. Bett, et al., *ACS Energy Letters* 8, no. 10 (2023): 4186.

20. Z. Wang, L. Zeng, T. Zhu, et al., *Nature* 618, no. 7963 (2023): 74.

21. F. Li, D. Wu, L. Shang, et al., *Advanced Materials* 36, no. 16 (2024): 2311595.

22. H. Hu, S. X. An, Y. Li, et al., *Energy & Environmental Science* 17, no. 8 (2024): 2800.

23. *Kaust Unveils Triple-Junction Perovskite-Perovskite-Silicon Solar Cell with 26.4*, accessed August 21, 2024, https://www.pv-magazine.com/2024/01/04/kaust-unveils-triple-junction-perovskite-perovskite-silicon-solar-cell-with-26-4-efficiency/.

24. S. Liu, Y. Lu, C. Yu, et al., *Nature* 628, no. 8007 (2024): 306.

25. L. Restat, C. Messmer, M. Heydarian, et al., *Solar RRL* 8, no. 5 (2024): 2300887.

26. I. Haedrich, U. Eitner, M. Wiese, and H. Wirth, *Solar Energy Materials and Solar Cells* 131 (2014): 14.

27. H. Liu, C. D. Rodríguez-Gallegos, Z. Liu, T. Buonassisi, T. Reindl, and I. M. Peters, *Cell Reports Physical Science* 1, no. 4 (2020): 100037.

28. M. Vogt, C. R. Tobon, A. Alcañiz, et al., *Solar Energy Materials and Solar Cells* 247 (2022): 111944.

29. L. A. Castriotta, M. Zendehdel, N. Yaghoobi Nia, et al., *Advanced Energy Materials* 12 (2022): 12.

30. L. Rakocevic, R. Gehlhaar, T. Merckx, et al., *IEEE Journal of Photovoltaics* 7, no. 1 (2017): 404.

31. F. Di Giacomo, L. A. Castriotta, F. U. Kosasih, D. Di Girolamo, C. Ducati, and A. Di Carlo, *Micromachines* 11, no. 12 (2020): 1127.

32. P. Zhu, C. Chen, J. Dai, et al., *Advanced Materials* 36, no. 15 (2024): 2307357.

33. X. Dai, S. Chen, Y. Deng, et al., *PRX Energy* 1, no. 1 (2022): 013004.

34. R. Guerrero-Lemus, R. Vega, T. Kim, A. Kimm, and L. Shephard, *Renewable and Sustainable Energy Reviews* 60 (2016): 1533.

35. R. Hezel, *Progress in Photovoltaics: Research and Applications* 11, no. 8 (2003): 549.

36. K. Jäger, P. Tillmann, E. A. Katz, and C. Becker, *Solar RRL* 5, no. 3 (2021): 2000628.

37. A. Onno, N. Rodkey, A. Asgharzadeh, et al., *Joule* 4, no. 3 (2020): 580.

38. M. T. Patel, R. Asadpour, J. Bin Jahangir, M. Ryyan Khan, and M. A. Alam, *Applied Energy* 329 (2023): 120175.

39. J. Lehr, M. Langenhorst, R. Schmager, et al., *Solar Energy Materials and Solar Cells* 208 (2020): 110367.

40. R. Santbergen, T. Meguro, T. Suezaki, G. Koizumi, K. Yamamoto, and M. Zeman, *IEEE Journal of Photovoltaics* 7, no. 3 (2017): 919.

41. R. Siegel, *Solar Energy* 15, no. 3 (1973): 273.

42. S. Manzoor, J. Häusele, K. A. Bush, et al., *Optics Express* 26, no. 21 (2018): 27441.

43. Y. Blom, M. Ruben Vogt, O. Isabella, and R. Santbergen, *Optics Express* 32, no. 3 (2024): 4365,

44. Y. Blom, *YBlom1999/InterpolationNK-YB: Final*, accessed August 21, 2024, https://doi.org/10.5281/zenodo.11367820.

45. A. W. Walker, O. Höhn, D. N. Micha, et al., *Journal of Photonics for Energy* 5, no. 1 (2015): 053087.

46. M. A. Steiner and J. F. Geisz, *Applied Physics Letters* 100 (2012): 25.

47. M. Z. Shvarts, M. A. Mintairov, V. M. Emelyanov, V. V. Evstropov, V. M. Lantratov, and N. K. Timoshina, *AIP Conference Proceedings* 1556 (2013): 147–151.

48. N. L. A. Chan, T. Thomas, M. Fuhrer, and N. J. Ekins-Daukes, *IEEE Journal of Photovoltaics* 4, no. 5 (2014): 1306.

49. M. Zeman, J. van den Heuvel, M. Kroon, et al., 2019. Advanced Semiconductor Analysis. Technical Report. Delft: University of Technology.

50. T. Jung, H. Song, H. Ahn, and G. Kang, *Solar Energy* 103 (2014): 253.

51. A. u. Rehman, E. P. Van Kerschaver, E. Aydin, W. Raja, T. G. Allen, and S. De Wolf, *Progress in Photovoltaics: Research and Applications* 31, no. 4 (2023): 429.

52. R. Witteck, H. Schulte-Huxel, H. Holst, et al., *Energy Procedia* 92 (2016): 531.

53. T. Moot, J. B. Patel, G. McAndrews, et al., *ACS Energy Letters* 6, no. 5 (2021): 2038.

54. A. Calcabrini, R. Cardose, D. Gribnau, et al., *Progress in Photovoltaics: Research and Applications* 31, no. 2 (2023): 134.

55. P. Ricchiazzi, S. Yang, C. Gautier, and D. Sowle, *Bulletin of the American Meteorological Society* 79, no. 10 (1998): 2101.

56. S. Mariotti, E. Köhnen, F. Scheler, et al., *Science* 381, no. 6653 (2023): 63.

57. C. Monokroussos, Q. Gao, X. Zhang, et al., *Progress in Photovoltaics: Research and Applications* 28, no. 8 (2020): 755.

58. M. Kottek, J. Grieser, C. Beck, B. Rudolf, and F. Rubel, *Meteorologische Zeitschrif* 15, no. 3 (2006): 259.

59. J. Ascencio-Vásquez, K. Brecl, and M. Topič, *Solar Energy* 191 (2019): 672.

60. J. Remund, S. Müller, M. Schmutz, and P. Graf, *METEOTEST*, 2020, www.meteotest.com.

61. M. H. Futscher and B. Ehrler, *ACS Energy Letters* 1, no. 4 (2016): 863.

Supporting Information

Additional supporting information can be found online in the Supporting Information section.